PROCEEDINGS, 44th Workshop on Geothermal Reservoir Engineering
Stanford University, Stanford, California, February 11-13, 2019
SGP-TR-214

Surface Deformation at the Heber Geothermal Field in Southern California

Mariana Eneva[1], David Adams[1], Vicky Hsiao[2], Giacomo Falorni[2] and Roberto Locatelli[3]

[1]Imageair Inc., 600 Greensburg Circle, Reno, NV 89509, USA

[2]TRE Altamira Inc., Suite 410, 475 West Georgia Street, Vancouver, BC V6B 4M9, Canada

[3]TRE Altamira s.r.l., Ripa di Porta Ticinese, 79, 20143 Milano, Italy

meneva@imageair-inc.com

Keywords: Heber, surface deformation, geothermal, InSAR, SqueeSAR, Envisat, Sentinel, subsidence, uplift

ABSTRACT

The Heber Geothermal Field is one of four operating geothermal fields in the Imperial Valley of southern California. The field represents a blind geothermal system located north of the border with Mexico, and south-southeast of the town of El Centro. The HGF has one double flash and three binary plants, with a total generating capacity of 120 MWe, and current production of ~90 MWe. As part of projects with the California Energy Commission (CEC), we have studied surface deformation at Heber using SqueeSAR, an interferometric synthetic aperture radar (InSAR) technique applied to Envisat (August 2005 – August 2010) and Sentinel (April 2015 – April 2018) satellite data. SqueeSAR is based on permanent and distributed scatterers, often aligned along roads and canals. This makes it possible to detect surface movements in vegetated areas where conventional InSAR techniques do not work. The spatial patterns and changes in time of surface deformation are related to changes in production and injection, and are confirmed by ground-based leveling data. Prominent subsidence is observed in both study periods, of up to −45 mm/year. In addition, after an increase in injection in 2005, uplift appears in some previously subsiding areas in the northeastern part of the field. This uplift is detected in the Envisat period, but gets reduced or resumes subsidence in the Sentinel period. In addition, horizontal movements are observed, following a pattern of westward displacements on the eastern flanks of subsidence areas and eastward displacements on the western flanks. Since surface deformation is dynamically connected to production and injection, and InSAR provides cost-effective and dense spatial and temporal coverage, such satellite measurements can greatly benefit field management and operations.

1. INTRODUCTION

The Heber geothermal field is located in the Imperial Valley of southern California (Figure 1) that is part of the Gulf of California rift zone. The valley extends for about 80 km from the southern shore of the Salton Sea toward the U.S.-Mexico border. It is also part of the Salton Through, which represents a spreading center due to the relative movement of the Pacific and North American Plates. This leads to active regional tectonics associated with high heat flow and volcanism (e.g., Lachenbruch et al. 1985), substantial subsidence and horizontal movements, localized deformation due to networks of strike-slip and normal faults, and surface displacements caused by numerous earthquakes and aseismic slip. Superimposed on the tectonically induced surface deformation are anthropogenic sources of surface changes, including the geothermal operations in southern California.

The high heat flow in the Salton Trough led to geothermal developments that currently produce a total of ~520 MWe (data from http://openEI.org/wiki and http://www.ormat.com), second only to The Geysers in the U.S. The current geothermal operations take place at the Salon Sea geothermal field (operated by CalEnergy Resources Ltd. in its central and southwestern parts, and by EnergySource LLC in its northeastern part), and at the Heber, North Brawley, and East Mesa (Ormesa) geothermal fields (all three operated by Ormat Technologies Inc.).

Heber represents a blind geothermal system (e.g., Lippmann and Bodvarsson, 1985) located just north of the border with Mexico, and south-southeast of the town of El Centro (Fig. 1). The field was first developed in the early 1980's by Chevron, starting with a double flashed plant. Initial output was lower than expected, so a modular binary power plant was added, making the geothermal operations successful since the mid-1993 (Sones and Krieger, 2000). At present, the field has one double flash and three binary plants, with a current production of 89 MWe (http://www.ormat.com) that is 17% of the total Imperial Valley geothermal production. Its estimated generating capacity is 120 MWe. The reservoir volume is estimated at 23 km^3 (Gawell, 2014) to 28 km^3 (Geothermex, 2004). The depths to the top and bottom of the reservoir are 1,200 m and 1,800 m, respectively (Sones and Schochet (1999). The mean temperature at depth has been reported at 375^{o}C (USGS, 2008), but the lower average temperature of the geofluids (174^{o}C) necessitated the construction of binary plants. It is assumed that the controlling structure is pull-apart, in a strike-slip fault zone, with a reservoir model including three major permeability units (James et al., 1987) – "capping" clays at depth of 150-150 m, high matrix permeability sandstone "outflow" reservoir at 150-1,680 m, and high permeability "feeder" faults and fractures in indurated sediments below 1,680 m. These were deduced from seismic lines, and maps and cross-sections of lost circulation and temperature distribution. James et al. (1987) also commented on a steep pressure decline under initial production, but subsequent rapid stabilization due to regional aquifer support. The authors concluded that the reservoir is very permeable and that there is a significant opportunity for additional development of the field. Allison (1990) used borehole breakout orientations to confirm these findings, particularly the right strike-slip and normal faults suggested by James et al. (1987).

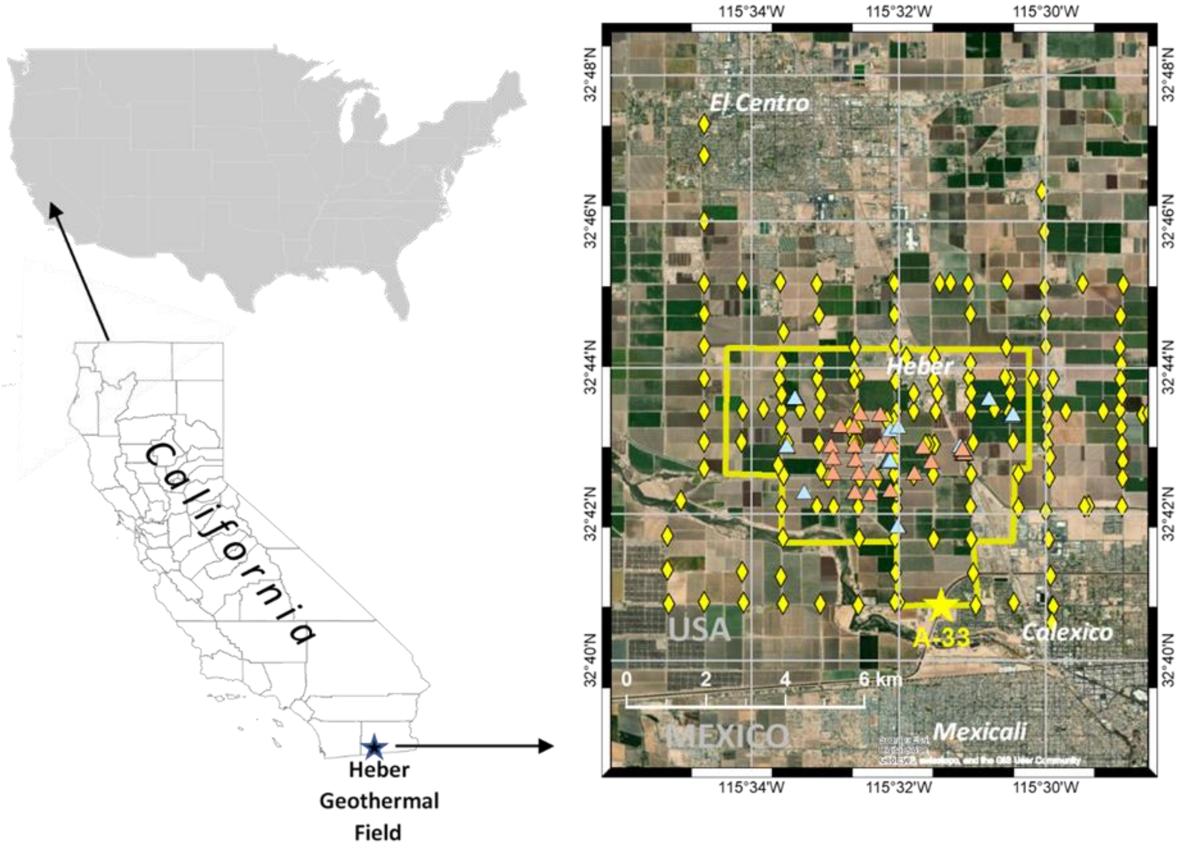

Figure 1. Map of the Heber geothermal field area. Yellow outline marks the known geothermal resource area (KGRA). Orange triangles – production wells. Blue triangles – injection wells. Yellow diamonds – benchmarks used in leveling surveys.

We have been investigating surface deformation in geothermal areas of California (Eneva et al., 2009-2018) in several projects with the California Energy Commission (CEC), with the intention to demonstrate its dynamic relationship to production and injection, which can be useful in reservoir management and operation. Surface deformation has been traditionally measured through ground-based leveling surveys and GPS. A more recent development, interferometric synthetic aperture radar (InSAR) has made it possible to measure surface displacements from space, providing cost-effective and dense spatial and temporal coverage. Agricultural areas like the Imperial Valley are largely inaccessible to earlier InSAR techniques. Using SqueeSAR (Ferretti at al., 2011), a state-of-the-art InSAR technique, we were able to measure for the first time from space surface deformation in the agricultural areas of the Imperial Valley, including at Heber (Eneva et al., 2013). This was possible because SqueeSAR is based on points that play the role of scatterers in the satellite images, which commonly align along roads and canals intersecting the agricultural areas. This leads to the detection of surface movements that are hidden to conventional InSAR techniques. Here we revisit our earlier findings (Eneva et al., 2013) and integrate them with continued analysis of new satellite data.

2. TECHNIQUE

InSAR makes use of a special type of satellite radar data, synthetic aperture radar (SAR). The first InSAR technique developed to detect surface deformation was differential InSAR (i.e., DInSAR) – see Eneva (2010) for an overview. Subsequent innovations, PSInSAR^{TM} (Ferretti, et al., 2007), and its extension, SqueeSAR^{TM} (Ferretti, et al., 2011), both developed at TRE Altamira, make it possible to detect deformation in vegetated areas where DInSAR does not work. SqueeSAR makes use of “permanent” and “distributed” scatterers (PS and DS). The PS points can be buildings, well pads, points along roads and canals, fences, lamp posts, transmission towers, rock outcrops, etc. They serve as reflectors of the radar waves that are consistently identified in a sequence of radar scenes, so that time series of surface deformation are derived at each individual PS. The DS represent homogeneous areas emitting signals with smaller signal-to-noise ratios than the PS, but still significantly above the background noise. They include rangelands, pastures, and bare earth that are frequently encountered in relatively arid environments and rural areas. The scatterer-based techniques typically provide deformation time series at thousands of locations (vastly exceeding the spatial coverage of leveling surveys and GPS networks), and multiple times per year (compared with annual, or less frequent, leveling surveys). We have previously applied PSInSAR and SqueeSAR to geothermal fields and other areas of southern California and northern Nevada (Eneva et al., 2009-2018; Ayling et al., 2018). In southern California we obtained results in some areas that were untapped by InSAR before. Hereafter, we use the more generic term “InSAR,” with which, unless stated otherwise, we mean the SqueeSAR technique.

In any InSAR technique, the deformation is first measured in the line-of-sight (LOS) to the satellite, with negative and positive LOS displacements indicating movements away from and toward the satellite, respectively. Deformation time series are obtained at each PS and DS point and are used to calculate annual deformation rates from the slopes of straight lines fitted to the time series. When these are obtained from both descending and ascending satellite images (i.e., satellite moving north to south and south to north, respectively), it is possible to decompose the two sets of LOS movements into vertical and horizontal components. The satellite orbital geometries of all past and current satellites with SAR instruments on board allow only the determination of the east horizontal component, while the north component cannot be recovered (e.g., Wright, et al., 2004). The SAR instruments are commonly right-looking, in direction perpendicular to the satellite trajectory, and downward under a relatively steep look (incident) angle from the vertical to the ground, especially for some of the satellites. This leads to LOS measurements that are generally more sensitive to the vertical displacements than to the east horizontal ones, so that as long as the horizontal movements do not exceed significantly the vertical movements, the LOS movements away from or toward the satellite are often indicative of subsidence or uplift, respectively. For this reason, the LOS and vertical deformation maps often display similar spatial patterns, although with different numerical values. In contrast, the pattern of the east horizontal movements is completely different and is only revealed after a decomposition. Due to differences in the orbital geometries (look and heading angles), LOS measurements from different satellites cannot be compared directly, unless the LOS of one satellite is projected onto the LOS of the other satellite. Therefore, it is more straightforward to use the vertical and east horizontal components that are readily comparable between satellites, and are easier to understand intuitively. On the other hand, these components are calculated in pixels; the estimates assigned to any given pixel are derived as an average from the LOS measurements at all individual ascending and descending scatterers in that pixel, so if data of one LOS type is missing, the pixel remains without vertical and east estimates. That is, there is a loss of information when transitioning from LOS to vertical and east components, which is smaller in dry areas (i.e., with dense distribution of scatterers), but could be substantial in vegetated areas where it is fairly common to identify scatterers in a given area from only one type of LOS and not from the other type.

The SqueeSAR measurements of deformation are relative to a reference point. Whenever possible, it is best to choose a reference point with a known movement (three-components from a GPS, or at least a vertical component from a leveling benchmark). For Heber, we use as a reference point the benchmark that is the datum in the annual leveling surveys in the field (A-33).

2. DATA

The data used in this study are SAR images from two satellites, monthly reports of the time series of injection and production, and reports from annual leveling surveys. The locations of the leveling benchmarks and wells are shown in Fig. 1

2.1 Satellite Data

The satellite data used in this study were acquired by two satellites, Envisat and Sentinel, covering two non-overlapping periods of time, with a gap of 4 years. Envisat data are generally available for InSAR processing between 2003 and October 2010, but the real periods of data availability vary from one area to another, and also, collection of images of one type of geometry (ascending in the case of Heber) may start significantly later than the other type. At Heber, ascending data become available in December 2003, but only three scenes were collected before August 2005. This limits the period for which decomposition into vertical and horizontal components can be done, as both types of LOS are needed, even though the descending time series starts earlier and is longer. Also, occasionally some scenes turn out to be unsuitable for InSAR and are dropped from the processing (six descending Envisat scenes were not included). In view of this and some other restrictions, the primary Envisat period investigated for Heber is five years, August 2005 – August 2010. The minimum frequency for the Envisat images is 35 days, due to the revisit time for any given location, but the interval between consecutive scenes could be multiples of this interval, as data may not be collected during each revisit.

Sentinel data are obtained from two satellites, Sentinel-1A (launched April 2014) and Sentinel-1B (launched April 2016), and continue to be collected. The initial revisit time of 24 days decreased with the launch of the second satellite, and starting in May 2017, it is 12 days. For Heber, Sentinel descending data are available since March 2015, and the descending data since April 2015, so we analyzed data from a three-year period, April 2015 – April 2018.

Table 1 shows the following parameters for the two satellites: periods of available data; study period; numbers of scenes of the two geometries, the θ and δ angles, and unit vectors (Up, East, and North). The look angle θ is the angle between the LOS and the vertical to the ground, and the heading angle δ is the angle formed with the geographic North. These parameters are shown for the two geometries, ascending and descending, marked with A and D, respectively. Each unit vector represents a measure of the sensitivity of the LOS measurements in a certain direction. It is evident that the highest sensitivity is to the vertical component and there is a fairly good sensitivity to the east horizontal component. The sensitivity to the north component is low for both satellites, precluding the detetion of northward or southward movements.

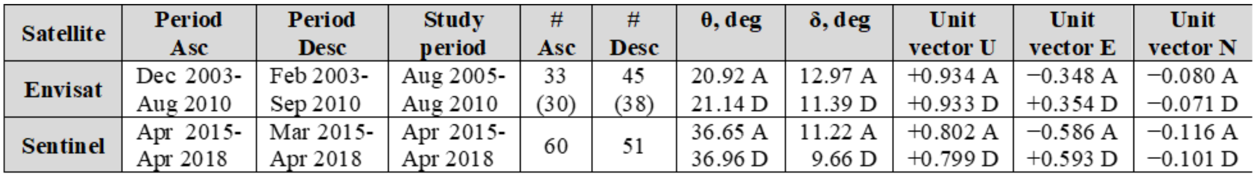

Satellite	Period Asc	Period Desc	Study period	# Asc	# Desc	θ, deg	δ, deg	Unit vector U	Unit vector E	Unit vector N
Envisat	Dec 2003- Aug 2010	Feb 2003- Sep 2010	Aug 2005- Aug 2010	33 (30)	45 (38)	20.92 A 21.14 D	12.97 A 11.39 D	+0.934 A +0.933 D	−0.348 A +0.354 D	−0.080 A −0.071 D
Sentinel	Apr 2015- Apr 2018	Mar 2015- Apr 2018	Apr 2015- Apr 2018	60	51	36.65 A 36.96 D	11.22 A 9.66 D	+0.802 A +0.799 D	−0.586 A +0.593 D	−0.116 A −0.101 D

Table 1. Parameters of the satellite data used in this study.

2.2 Well Data

Time series of the monthly fluid amounts from individual production and injection wells are available from the Division of Oil, Gas, and Geothermal Resources (DOGGR) of the California Department of Conservation (DOGGR, 2018). These data go back to 1985. Figure 2 shows maps of ascending LOS rates (to be discussed in more detail below), on which the well locations are superimposed. Figure 3 shows examples of monthly fluid volumes from several injection and production wells, specifically chosen in relation to the surface deformation patterns depicted in Fig. 2.

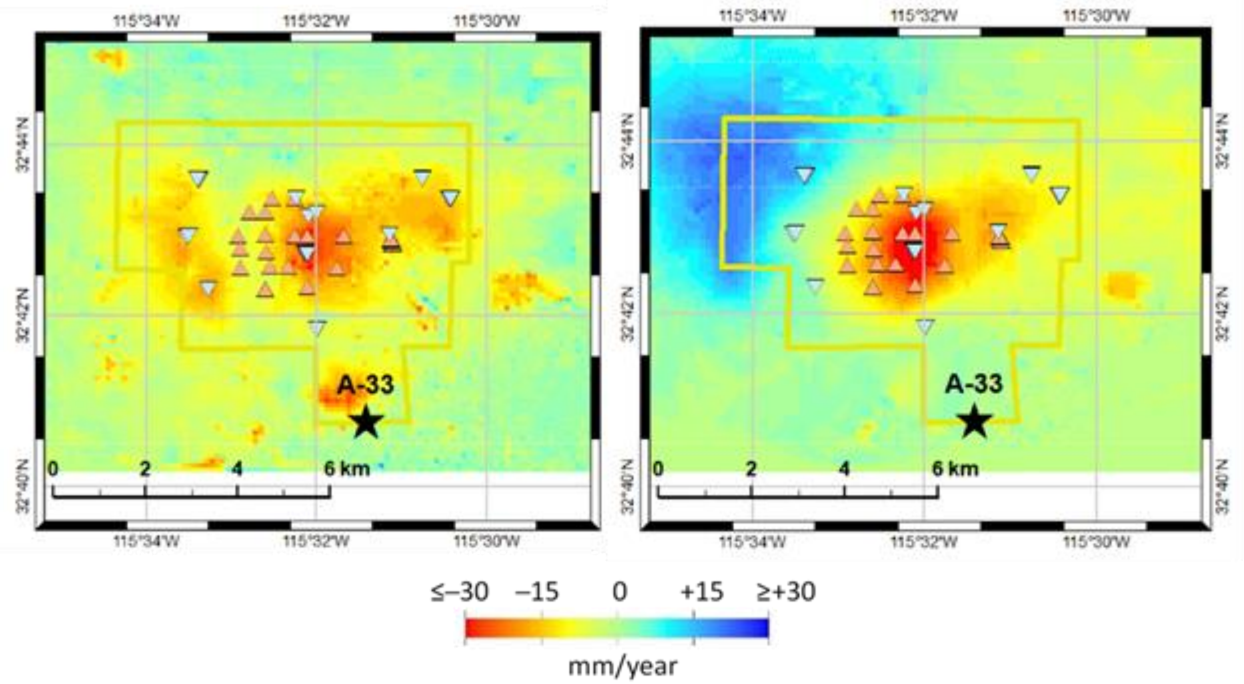

Figure 2. Maps showing ascending LOS deformation rates and well locations. Left: Sentinel data. Right – Envisat data. Yellow outline – Heber KGRA. Orange triangles – production wells. Blue inverted triangles – injection wells. Black star – benchmark used as datum in the leveling surveys and as a reference point in the InSAR processing. Yellow to red areas – subsidence. Blue areas – uplift.

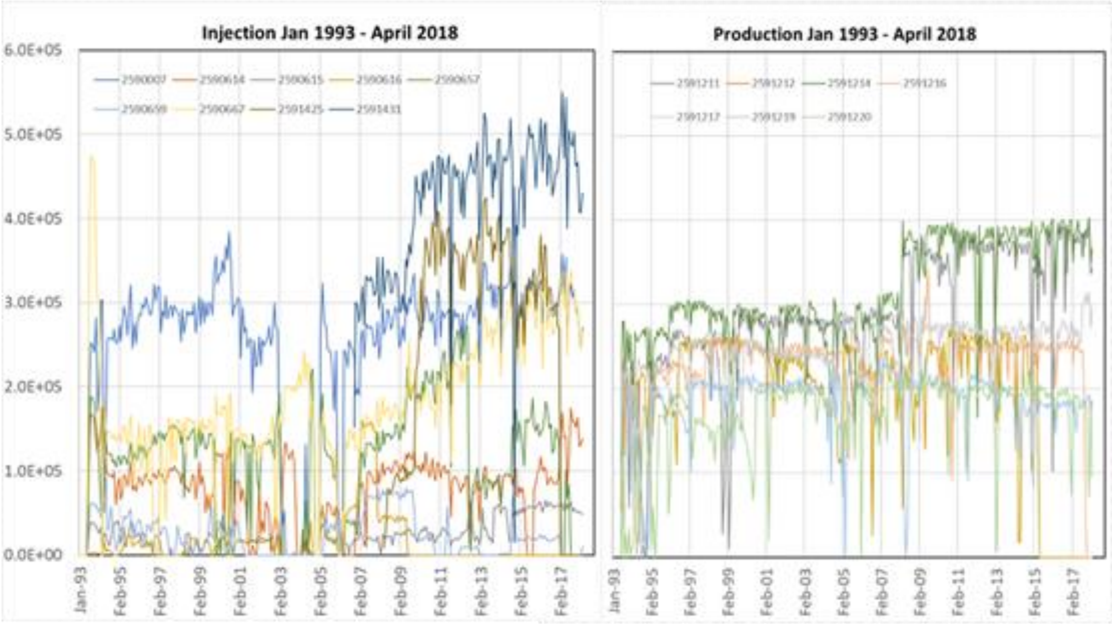

Figure 3. Monthly fluid amounts (in kg). Left – time series for injection wells in the area showing uplift in the Envisat period. Right: time series for production wells in the subsidence area at the center of the field. Legends show API numbers of the wells.

The number of injection wells at Heber is 37. Some of these are clustered, so the maps in Figs. 1 and 2 show only 11 distinct injection locations or clusters. The monthly injected amounts shown in the plot on the left in Fig. 3 are from the wells in the western part of the Heber KGRA. They are located in or near an area of uplift during the Envisat period, in the northwesternmost part of the field. However, in the Sentinel period this area is subsiding. Significant rapid increase in injection is seen for some of these wells, starting in 2005 (when Ormat took over) or later. The fluid amounts eventually increase more slowly or level out around 2011-2013.

The number of production wells since 1985 is 41, of which 29 wells were active during the Envisat and/or Sentinel periods, and three additional wells worked only in the gap between the two periods. Because some of the wells are very close to each other, the map in Fig. 1 displays only 18 distinct locations and clusters. Eight production wells operating in 1985-1988 were later turned into injection wells that are active during the study periods. One more well was production in the period July 1993 - May 2015, stopped for 8 months, and then continued as an injection well since February 1916; this is the only well that switched type during one of our study periods. The plot to the right in Fig. 3 shows fluid time series for several production wells from around the center of the field, where continued subsidence is observed in both study periods. It is evident that the production from some of those wells was ramped up in 2008.

2.3 Data from Leveling Surveys

Geothermal operators in Imperial Valley are obligated to provide data from annual leveling surveys to the Imperial County Department of Public Works (ICDPW), which makes them available to our project. We have been using these data for comparison with the InSAR measurements. The number of benchmarks changes over the years; as of 2018 there are data for 145 benchmarks. The last survey for which we have data was performed in January 2018. The benchmark locations at and around Heber are shown in Fig. 1. Figure 4 shows representative examples of time series from several benchmarks taken from the same areas as the wells, whose monthly fluid volumes were shown in Fig. 3. The group of benchmarks from the center of the field indicates substantial ongoing subsidence (on the right in Fig. 4), increasing after 2005. The other group, from the western and northwestern part of the field, show subsidence until about 2005, then uplift after Ormat took over and injection was ramped up (as seen in Fig. 3-left), followed by leveling or resumed subsidence since about 2010. The last data points from January 2018 appear to indicate either decreasing subsidence, leveling, or even trend reversals. Until the next annual leveling survey is carried out, it will not be clear if this is an enduring trend. However, later in this project, we will analyze Sentinel satellite data for the period after May 2018. At a 12-day revisit frequency, there will be a substantial number of scenes (i.e., data points), which may indicate if there is indeed change in the deformation rates in this area.

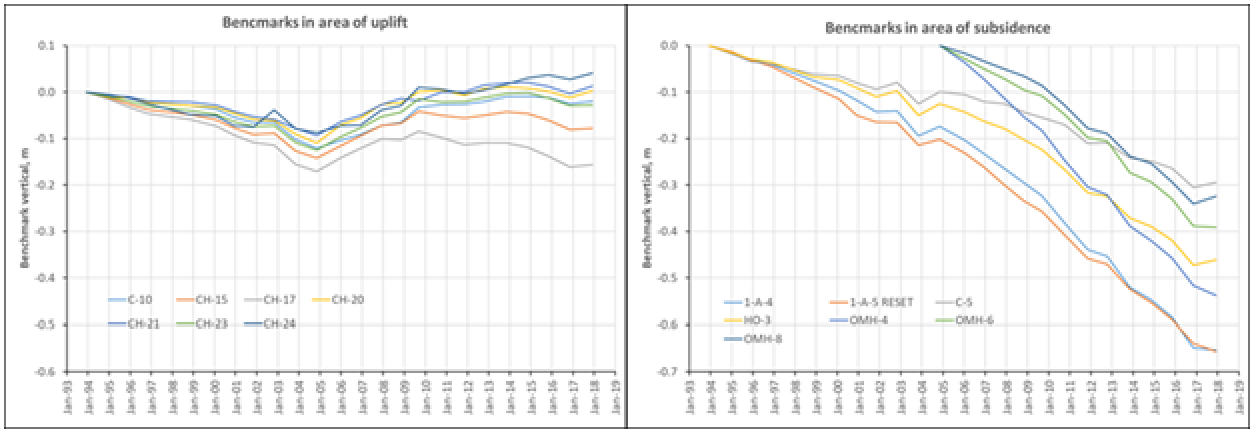

Figure 4. Time series of deformation from leveling surveys. Left – Benchmarks in the area of uplift in the Envisat period. Right – benchmarks in the area of maximum subsidence. Legends show benchmark names.

3. RESULTS

The following figures and tables show more detailed examples of results from our ongoing study. Table 2 shows the numbers of ascending and descending PS and DS points in a ~450 km^2 extended area around Heber. Sentinel data are significantly more numerous than the Envisat data. The data processing provides a time series for each individual scatterer. The vertical and east horizontal rates are calculated in 100-m pixels from the ascending and descending rates within those pixels. The last column of Table 2 shows how many of the pixels are with such decomposed values. The remaining pixels do not have estimates, because either there were no LOS measurements in them, or there were only measurements of one LOS type (descending or ascending, but not both).

Satellite	**Num Asc PS/DS**	**Num Desc PS/DS**	**Num 100-m pixels (Vert/East)**
Envisat	39,185	25,716	5,402 (of 44,460) – 12.2%
Sentinel	94,215	104,483	16,772 (of 44,460) – 37.7%

Table 2. Numbers of scatterers and pixels used in the study.

Even though the number of PS and DS points is much larger than the number of benchmarks (145), and there are many such points where benchmarks are absent, the opposite is also observed - there are benchmarks in areas devoid of scatterers. This can be overcome by installing corner reflectors (e.g., Garthwaite et al., 2015) at points of interest, such as where the maximum subsidence is expected.

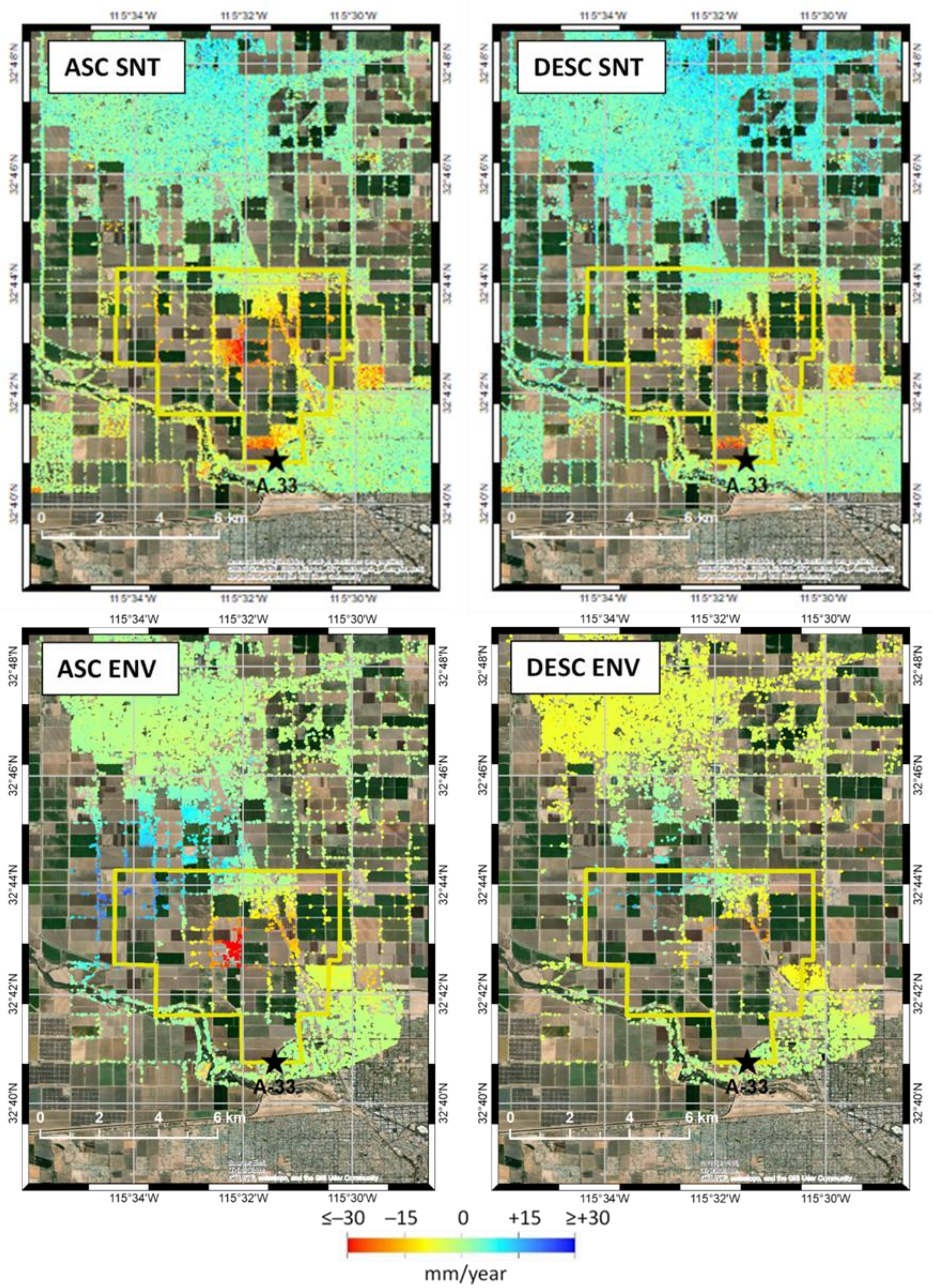

Figure 5. Maps of ascending (left) and descending (right) LOS rates obtained from the Sentinel (top) and Envisat (bottom) images.

The corner reflectors would be identified in both the ascending and descending LOS, thus ensuring the capability of estimating the vertical and east horizontal rates where it is of most interest.

Negative values are used for LOS movements away from the satellite, subsidence, and westward horizontal displacements. Positive values are used for LOS movements toward the satellite, uplift, and eastward horizontal displacements. Figure 5 shows the PS/DS locations, color coded according to the LOS rates of deformation (slopes of straight lines through the time series). Movements away from the satellite, likely associated with subsidence, are marked in yellow to red colors, and are with negative rates. Blue colors (positive values) indicate displacements toward the satellite, likely related to uplift.

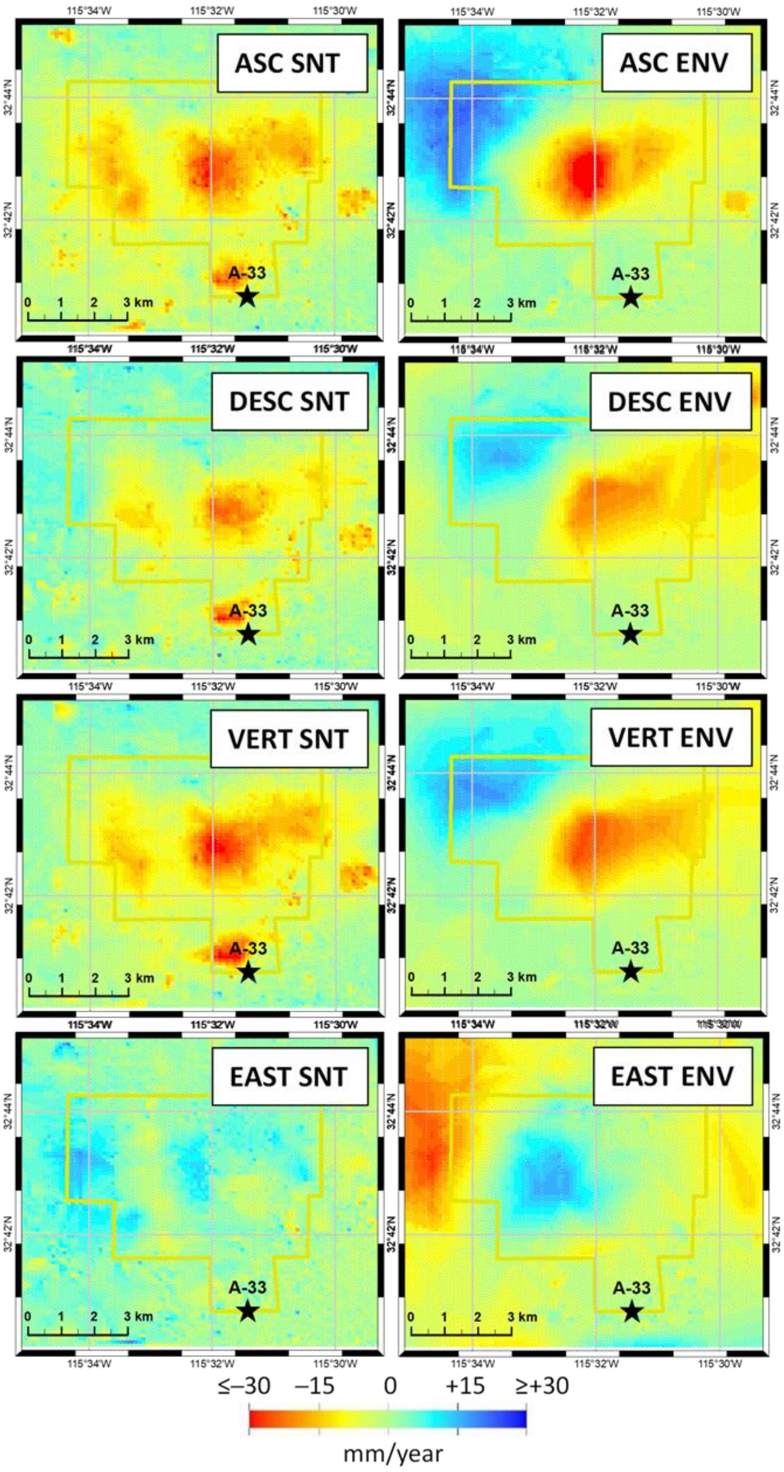

Figure 6. Maps of linearly interpolated deformation rates as indicated. Other notations as in previous figures.

Figure 6 shows a complete set of maps of linearly interpolated values from the LOS and Vertical/East rates (the two plots on the top are the same as those in Fig. 2, without the wells). This rendition of the data shows more clearly the major difference already gleaned from the point measurements in Fig. 5 – compared with the Sentinel data, the Envisat data show a significant uplift to the northwest. Otherwise, subsidence from the center of the KGRA and extending to the northeast, is seen in both periods, covering an area of size ~ 5 km x 3 km. This confirms the observations from the benchmarks in the uplift (Envisat only) and subsidence areas (Fig. 4). During the Sentinel period, the Envisat uplift apparently turns into subsidence, extending also to the south and southeast of the previously uplifting area. Changes are also seen in the horizontal movements (plots on the bottom). During the Envisat period, there are eastward displacements to the west of the central subsidence area, and westward movements to the west and northwest of the uplift area. The pattern is different in the Sentinel period – there are several transitions between eastward and westward displacements, generally pointing toward the inner parts of the subsidence areas; i.e., the western flanks of subsidence areas tend to move eastward and the eastern flanks tend to move westward.

Satellite	Max Asc, mm/yr	Max Desc, mm/yr	Max Vert, mm/yr	Max East, mm/yr
Envisat	−44.9; +24.3 (±4.1)	−30.7; +17.4 (±2.8)	−26.7; +18.8 (±3.1)	−29.6; +17.8 (±4.7)
Sentinel	−44.1; +29.7 (±5.5)	−40.5; +4.3 (±5.5)	−38.1; +23.3 (±5.5)	−19.9; +25.9 (±3.4)

Table 3. Observed maximum rates. Negative values: away from satellites, subsidence, or westward. Positive values: toward satellite, uplift, or eastward. Standard deviations in parentheses.

Table 3 shows the maximum displacement rates measured from the two satellites. Note that these measurements are not necessarily at the same points, and not always depict the true maximum values, as there may not be scatterers at those locations. The area of maximum subsidence is "seen" better in the Envisat ascending LOS than the descending one. Therefore, due to lack of data, the Envisat maximum observed descending LOS and vertical rates do not capture the maximum subsidence, and the estimates in the table are from the periphery of the subsidence area. For this reason, the maximum ascending rates are more representative of the true maximum subsidence, which can be assumed to be around −45 mm/year. Similarly, the maximum uplift was likely around 20-25 mm/year.

It is usually assumed that surface deformation should not be observed around binary plants, because of the almost 100%-reinjection of the produced fluids. Our results show that this is not the case, and that both subsidence and uplift are observed at Heber that change dynamically with changes in production and injection. The maximum subsidence rate is actually comparable with that from the Salton Sea geothermal field (Eneva et al., 2014), where flash plants are installed. Even in that case, the reinjection is pretty high, at 82% on average. While the observed rates of surface deformation may appear high, without such significant levels of reinjection, the displacements would have been significantly larger. This is exemplified by the Cerro Prieto geothermal field, to the south in Mexico, where a reinjection strategy is either absent or insufficient, and the maximum subsidence is much larger, at −170 mm/year in a recharge area next to the field, and −110 mm/year in the producing area (Sarychikhina et al., 2011).

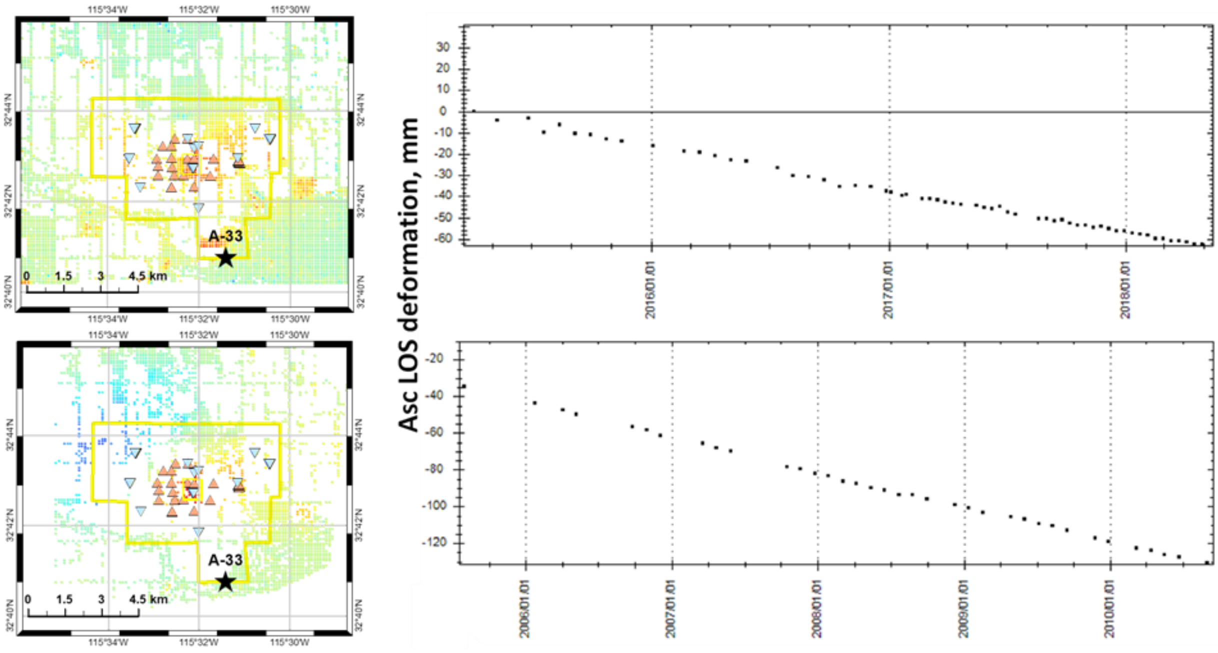

Figure 7. Average time series of ascending LOS deformation from the central subsidence area. Top – Sentinel. Bottom – Envisat.

In support of these observations, Figure 7 shows examples of time series from the two periods averaged over a small, ~ 1 km^2 area within the larger subsidence area, as depicted by the ascending LOS rates. The LOS ascending rates from these averaged time series are similar for both periods, −18 to −20 mm/year. Furthermore, Figure 8 shows the progression of deformation along a profile that intersects both the uplift area to the northwest seen in the Envisat period and the subsidence area present in both the Envisat and Sentinel periods. The thickness of the profile, 2.5 km, captures more clearly the uplift and subsidence, compared with a thinner profile passing through the maximum that would enclose very few data points. This leads to smaller cumulative subsidence and uplift, as compared with the maximum rates. Comparing the Envisat and Sentinel periods, Fig. 8 demonstrates the absence of uplift to the northwest, as well as continuing, but reduced subsidence at the center of the field.

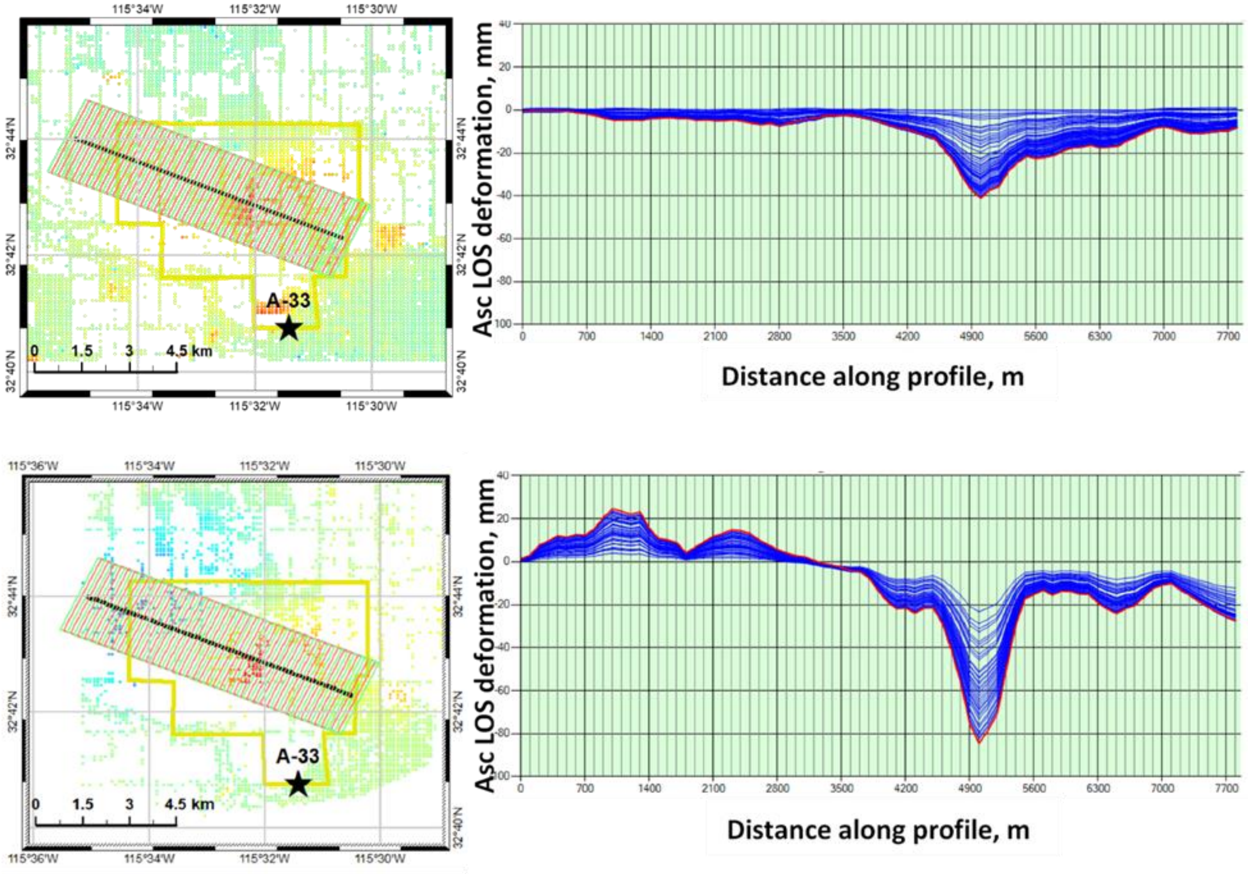

Figure 8. Progression of the ascending LOS deformation along a profile spanning the Heber geothermal field.

Another way to compare the two periods is on a pixel-to-pixel basis. Figure 9 displays the Envisat vertical rates versus the Sentinel ones, for pixels that have measurements from both periods. In this case, the comparison is from a much smaller area, of size ~45 km^2, that encloses the Heber KGRA (i.e., without extending to El Centro to the north). In that area, 734 100-m pixels have both measurements. If the measurements spanning both periods are similar, the points in Fig. 9 would cluster around the yellow dashed line in the plot. We see some of this tendency in the lower left quadrant, where the pixels with subsidence in both periods are clustered. These pixels are from the subsidence bowl in the center of the field. Still, more points are below the yellow line than above it, indicating larger subsidence in the earlier Envisat period for the same pixels. In contrast, points above the horizontal axis are related to the pixels with uplift in the Envisat period. Several of the points with the largest uplift in the Envisat data exhibit subsidence in the Sentinel period (upper left quadrant). Other pixels that experienced uplift in the Envisat period, still show uplift in the Sentinel period, but at a much lower rate (upper right quadrant); once the rates fall below +5 mm/year, they are comparable with the standard deviation (see Table 3).

4. CONCLUSIONS

The observations described here demonstrate the value of InSAR in providing a cost-effective and dense spatial and temporal coverage for the measurement of surface deformation in geothermal fields. The scatterer-based SqueeSAR technique employed here makes it possible to estimate surface deformation in agricultural areas that were not accessible to earlier InSAR techniques.

Using data from two satellites, Envisat and Sentinel, we observe changes in surface deformation at the Heber geothermal field, corresponding to changes in production and injection. Subsidence at the center of the field is observed in both study periods, August 2005 – August 2010 and April 2015 – April 2018, while a significant uplift is observed to the northwest of the subsidence bowl during the earlier period, but not in the later period. This is also confirmed by data from leveling surveys. Based on the apparent capability of InSAR to capture the dynamics of surface deformation, we suggest that it would be very beneficial to integrate such satellite measurements in the geothermal operation strategies.

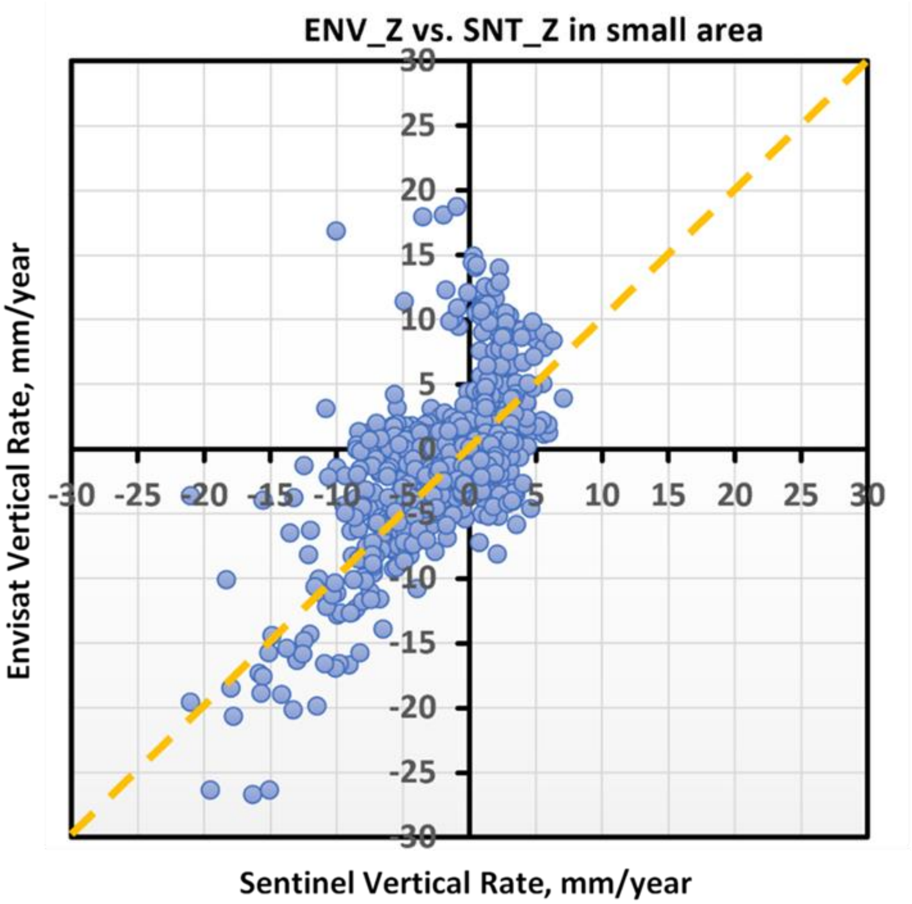

The results reported here are part of ongoing work that is in the process of including deformation modeling and analysis of the scarce seismicity in the area, which nonetheless appears to be also related to changes in injection and production. In the near future, these two elements will be integrated with the surface deformation; it is expected that their joint application will significantly contribute to reservoir management.

ACKNOWLEDGMENTS

This work is part of a current project with the California Energy Commission (CEC), GEO-16-003. It also uses data from a previous CEC project, GEO-10-001. We thank the CEC Technical Manager, Elisabeth de Jong, for support throughout the project. We also thank John Gay, Veronica Atondo, and Guillermo Mendoza from the Imperial County Department of Public Works (IVDPW) for assisting us with obtaining the leveling survey data.

REFERENCES

Allison, M.L.: Remote Detection of Active Faults Using Borehole Breakouts in the Heber Geothermal Field, Imperial Valley, California, *Geothermal Research Council Transactions*, **14**, (1990), 1359-1364.

Ayling, B. and the Fallon FORGE team (36 co-authors).: Phase 2 Update for the Fallon FORGE Site, Nevada, USA, *PROCEEDINGS, 44th Workshop on Geothermal Reservoir Engineering*, Stanford University, Stanford, CA, (2018), SGP-TR-213.

Division of Oil, Gas, and Geothermal Resources - http://www.conservation.ca.gov/dog/; DOGGR website accessed December, 2018.

Eneva, M., Barbour, A., Adams, D., Hsiao, V., Blake, K., Falorni, G., and Locatelli, R.: Satellite Observations of Surface Deformation at the Coso Geothermal field, California, *Geothermal Resources Council Transactions*, **42**, (2018), 1383-1401.

Eneva, M., Adams, D., Falorni, G., Novali, F., and Hsiao, V.: Surface Deformation at the Salton Sea Geothermal Field from High-Precision Radar Interferometry, *Geothermal Resources Council Transactions*, **38**, (2014), 991-999.

Eneva, M., Adams, D., Falorni, G., and Morgan, J.: Application of Radar Interferometry to Detect Subsidence and Uplift at the Heber Geothermal Field, Southern California, *Geothermal Resources Council Transactions*, **37**, (2013), 491-499.

Eneva, M., Adams, D., Falorni, G., and Morgan, J.: Applications of Radar Interferometry to Detect Surface Deformation in Geothermal Areas of Imperial Valley in Southern California, *Proceedings*, 38th Workshop on Geothermal Reservoir Engineering, Stanford University, Stanford, CA (2013), SGP-TR-198.

Eneva, M., Adams, D., Falorni, G., and Morgan, J.: Surface Deformation in Imperial Valley, CA, from Satellite Radar Interferometry, *Geothermal Resources Council Transactions*, **36**, (2012), 1339-1344.

Eneva, M., Falorni, G., Teplow, W., Morgan, J., Rhodes,G., and Adams, D.: Surface Deformation at the San Emidio Geothermal Field, Nevada, from Satellite Radar Interferometry, *Geothermal Resources Council Transactions*, **35**, (2011), 1647-1653.

Eneva, M.: Detection of Surface Deformation at Mining and Geothermal Sites Using Satellite Radar Interferometry (InSAR), *Proceedings,* 44th U.S. Rock Mechanics Symposium and 5th U.S. – Canada Rock Mechanics Symposium, Salt Lake City, UT (2010).

Eneva, M., Falorni, G., Adams, D., Allievi, J., and Novali, F.: Application of Satellite Interferometry to the Detection of Surface Deformation in the Salton Sea Geothermal Field, California, *Geothermal Resources Council Transactions*, **33**, (2009), 315-319.

Ferretti, A., Fumagalli, A., Novali, F., Prati, C., Rocca, F., and Rucci, A.: A New Algorithm for Processing Interferometric Data-Stacks: SqueeSAR." *IEEE Trans. Geosc. Remote Sensing*, **49**(9), (2011), 3460-3470.

Ferretti, A., Savio, G., Barzaghi, R., Borghi, A., Musazzi, S., Novali, F., Prati, C. and Rocca, F.: Submillimeter Accuracy of InSAR Time Series: Experimental Validation, *IEEE Trans. Geosc. Remote Sensing*, **45**, (2007) 1142-1153.

Gawell, K.: Statement Before the Senate Select Committee on California's Energy Independence & Assembly Select Committee on Renewable Energy Economy in Rural California. Personal Communication sent to Senate Select Committee on California's Energy Independence & Assembly Select Committee on Renewable Energy Economy in Rural California, (2014).

Garthwaite, M.C., Sarah Lawrie, S., Dawson, J., and Thankappan, M.: Corner Reflectors as Tie Between InSAR and GNSS Measurements: Case Study of Resource Extraction in Australia, *Proceedings*, Fringe Workshop, Frascati, Italy, (2015), ESA SP-731.

Geothermex Inc.: New Geothermal Site Identification and Qualification, Richmond, CA, California Energy Commission. Report No.: P500-04-051, (2004), Contract No.: 500-04-051.

James, E.D., Hoang, V.T, and Epperson, I.J.: Structure, Permeability and Production Characteristics of the Heber, California Geothermal Field, *Proceedings*, 12th Workshop Geothermal Reservoir Engineering, Stanford, California, (1887), 267-271.

Lachenbruch, A.H., Sass, J.H., and Galanis, S.P.: Heat Flow in Southernmost California and the Origin of the Salton Trough, *Journal of Geophysical Research*, **90**, (1985), 6709-6736.

Lippmann, M.J. and Bodvarsson, G.S.: The Heber Geothermal Field, California: Natural State and Exploitation Modeling Studies, *Journal of Geophysical Research*, **90**, B1, (1985).

Sarychikhina, O., Glowacka, E., Mellors, R., and Suarez, V.F.: Land Subsidence in the Cerro Prieto Geothermal Field, Baja California, Mexico, from 1994 to 2005. An Integrated Analysis of DInSAR, Leveling, and Geological Data, *Journal of Volcanology and Geothermal Research*, **204**, (1-4), (2011), 76-90, doi: 10.1016/j.jvolgeores.2011.03.004.

Sones, R. and Krieger, Z.: Case History of the Binary Power Plant Development at the Heber, California Geothermal Resource, *Proceedings*, World Geothermal Congress, Kyushu – Tohoku, Japan, (2000), 2217-2219.

Sones, R. and Schochet D.N.: Binary Geothermal Power Plant Development at the Heber, California Geothermal Resource Area, *Geothermal Research Council Transactions*, **23**, (1999), 93-97.

U.S. Geological Survey: Assessment of Moderate- and High-Temperature Geothermal Resources of the United States, U.S. Geological Survey Fact Sheet 2008-3082 (2008).

Wright, T.J., Parsons, B.E., and Lu, Z.: Toward Mapping Surface Deformation in Three Dimensions Using InSAR, *Geophys. Res. Lett.*, **31**, (2004), L01607, doi:10.1029/2003GL018827.